

Crystal plasticity-inspired statistical analysis of dislocation substructures generated by continuum dislocation dynamics

Peng Lin^{1,2}, Vignesh Vivekanandan¹, Gustavo Castelluccio³, Benjamin Anglin⁴, Anter El-Azab¹

¹ Purdue University, West Lafayette, IN 47907, USA

² Now at Beihang University, Beijing, 100191, China

³ Cranfield University, Bedfordshire MK43 0AL, UK

⁴ Naval Nuclear Laboratory, West Mifflin, PA 15122, USA

Abstract:

A computational approach has been developed for analyzing the characteristics of 3D dislocation substructures generated by the vector-density based continuum dislocation dynamics (CDD). In this CDD framework, the dislocation density on the individual slip systems is represented by vector fields with a unique dislocation line direction at each point in space. The evolution of these density fields is governed by a set of transport equations coupled with crystal mechanics. Such a detailed picture of the dislocation system enables mesoscale plasticity simulations based on dislocation properties. Here, a computational approach based on streamline construction is proposed to obtain the characteristics of dislocation substructures generated by CDD. Streamlines are obtained by travelling along the tangent of the vector density and velocity fields of the dislocation system, and can be used to construct the dislocation lines and their paths in the deformed crystal in 3D. As explained in the text, the streamlines are computed by solving a set of partial differential equations. Here we use this approach to extract microstructure parameters from the CDD simulations that are relevant to substructure-sensitive crystal plasticity models. These parameters include the average mean free path and mobile dislocation segment length, as well as the dislocation wall volume fraction, and the corresponding distributions. The results show that both the mobile dislocation segment length and dislocation mean free path decrease with the applied strain, which is consistent with the models used in the literature, and that the mobile dislocation segment length follows a log-normal distribution.

Keywords: Continuum dislocation dynamics; Crystal plasticity; Dislocation substructure; Dislocation mean free path; Data mining

1 Introduction

The mechanical response of metallic material depends on a hierarchy of deformation mechanisms across multiple lengths scales. At the atomic scale, solid solution strengthening increases the shear stress required for dislocations to glide. At the mesoscale, dislocation interactions and patterning of sessile structures account for most of the strain hardening. Indeed, many researchers (Hansen et al., 2006; Hansen and Huang, 1998) have shown a correlation between the dislocation substructure formation and hardening, which has its origin in limiting the motion of mobile dislocations via both short range and long range interactions. In his seminal work, Mughrabi (1983) characterized the role of dislocation substructures on cyclic hardening and proposed the composite model in which the material is occupied by elastic walls formed by densely populated dislocations structures. The volume in between walls (so-called channels) is relatively dislocation free, which enables unobstructed glide of mobile dislocations. This model has been widely embraced to reproduce the Bauschinger effect from the internal stresses (or back stress) induced by dislocation structures (Mughrabi, 1983).

Estrin et al. (1998) further considered the composite model to model the mechanical response under large monotonic strains by modelling the volume fraction occupied by sessile dislocation walls. This work introduced the notion that the wall fraction (f_w) decreases with increase plastic shear strain (γ) according to,

$$f_w = f_{inf} + (f_0 - f_{inf}) \exp\left(\frac{-\gamma}{\bar{\gamma}}\right), \quad (1)$$

in which f_{inf} is the wall volume fraction at a suitably large strain, f_0 is the peak wall volume fraction and $\bar{\gamma}$ is a material constant that scales the rate of decay of f_w . As a result of the reduction in the wall fraction upon plastic shear, the hardening rate decreases as demonstrated by experiments. In the context of crystal plasticity, Sauzay (Sauzay, 2008) used the composite model to propose an analytical back stress formulation that relies on the Eshelby inclusion formalism under the infinitesimal strains and linear elasticity. Following this work, Castelluccio and McDowell (2017) further proposed a mesoscale-sensitive crystal plasticity model that parameterize dislocation substructures to predict the mechanical response of face centered cubic (FCC) metallic materials. This work introduced a crystallographic back stress rate (\dot{B}^α) proportional to the crystallographic shear rate ($\dot{\gamma}^\alpha$) such that,

$$\dot{B}^\alpha \propto \frac{f_w}{1-f_w} \dot{\gamma}^\alpha, \quad (2)$$

in which the wall fraction decreases with increasing the plastic shear range ($\Delta\gamma^{max}/2$),

$$f_w = f_{inf} + (f_0 - f_{inf}) \exp\left(\frac{-\Delta\gamma^{max}/2}{g_p}\right), \quad (3)$$

which is similar to the formulation proposed by Estrin et al. (1998). In Eq. (3), g_p is a fitting parameter. The work by Castelluccio and McDowell (2017) further relies on the similitude principle (Sauzay and Kubin, 2011),

$$d_{struc} \propto \tau^{-1}, \quad (4)$$

to quantify the wall spacing (d_{struc}) in terms of the resolved shear stress (τ), which is taken as the mobile dislocation segment length ($d_{struc} \cong l_{mobile}$). This length scale is further related to the dislocation mean free path (l_{free}) through the mesoscale parameter,

$$\eta = l_{free}/l_{mobile}, \quad (5)$$

which corresponds to the ratio of the dislocation mean free path to mobile dislocation segment length. These formulations predict the evolution of f_w , l_{free} , and l_{mobile} for any crystallographic orientation and plastic strain, but they require proper parameterization, which was obtained from the analysis of extensive transmission electron microscopy (TEM) images.

Castelluccio and McDowell (2017) further demonstrated that the proper quantification of mesoscale attributes (f_w , l_{free} , and l_{mobile}) results in an powerful modelling tool to describe the response of single and polycrystals. Indeed, the morphology of substructures, which depend on the crystallographic orientation, is well suited to estimate the anisotropic mean free path of mobile dislocation as highlighted by Devincre et al. (2008). A second notable advantage of substructure-sensitive models is that mesoscale length scales can be directly compared to TEM experiments. Other approaches, such as those based on the formation of dislocation junctions (Grilli et al., 2018) and geometrical necessary dislocations (GNDs) (Jiang et al., 2015), rely on highly uncertain dislocation density measurements and are more difficult to validate at a local level. Hence, the lack of uniqueness in crystal plasticity parameters, which is well known and difficult to address (Ashraf and Castelluccio, 2021) can be mitigated by constructing models that are validated across multiple length scales independently. In this case, validation occurs not only from the comparison with the homogenized stress-strain response, but also from the predicted wall spacing and volume fraction. Despite its success, the composite mode requires the quantification of the volume occupied by

regions of highly localized dislocation densities, which varies upon loading and for each crystallographic orientation. As a result, its generalization into general loading conditions has been limited to the availability of TEM experimental data.

Recent approaches have aimed at avoiding the need for extensive experimental data by implementing bottom-up computational models that can inform crystal plasticity models. For example, discrete dislocation dynamics (DDD) has been used to investigate dislocation cooperation phenomena at nano- and micron-scales (Csikor et al., 2007; Cui et al., 2014; Stricker et al., 2018; Stricker and Weygand, 2015). In terms of dislocation substructures, Lavenstein and coworkers (2019) used DDD to study the localization of edge dislocations in sessile walls. Similarly, Wu and Zaiser (2021) used DDD models to parameterize the evolution of the dislocation wall spacing and thickness, both of which can be used to inform crystal plasticity models. Despite the success of DDD models, their intense computational demands limit the spatial and time span of simulations, which affect the resulting substructure patterning. Hence, the bridging of DDD to engineering crystal plasticity models remains an open problem. Continuum dislocation dynamics (CDD) provides an alternative to DDD. CDD reduces the computational burden by using density field variables to track the evolution of curved dislocation line ensembles. The origin of CDD can be traced back to the introduction of the dislocation density tensor α by Nye (1953) and Kröner (1958) and its rate $\dot{\alpha} = \nabla \times (\mathbf{v} \times \alpha)$ formulated by Mura (1963) and Kosevich (1965), with \mathbf{v} being the dislocation velocity. Several authors have recently developed different CDD frameworks, see Arsenlis et al. (2004), Reuber et al. (2014), Leung et al. (2015), Hochrainer (2015), and Monavari and Zaiser (2018). Of the CDD models currently available, those by Xia and El-Azab (2015), Xia et al. (2016), Lin and El-Azab (2020), Lin et al. (2021b, 2021a) and Vivekanandan (2021) are relevant and will be used here to accomplish the task of connecting dislocation dynamics (DD) with crystal plasticity.

In analyzing DD datasets to extract information relevant to crystal plasticity the complexity of the dislocation network becomes an issue. As such, there is a growing demand for suitable algorithms of analysis of the dislocation networks. A data-mining approach has been proposed by Song et al. (Song et al., 2021) to express the strain energy density of a dislocation system as a function of dislocation density field variables and as a function of the coarse graining voxel size. A systematic coarse-graining analysis of DDD simulations have been presented recently

(Akhondzadeh et al., 2021, 2020) to formulate a generalized Taylor relation and a generalized Kocks-Mecking model. Machine learning models also have been used to deduce the dislocation characteristics from large sets of dislocation dynamics simulations (Rafiei et al., 2020; Steinberger et al., 2019; Yang et al., 2020).

The current work establishes a data-mining approach to characterize mesoscale attributes (f_w , l_{free} , and l_{mobile}) relevant to crystal plasticity using CDD simulations. We consider the dislocation evolution formulated by Xia and El-Azab (Xia and El-Azab, 2015), in which dislocations on various slip systems are represented by vector fields weighted by their corresponding crystallographic Burgers vectors. The direction of the dislocation for each slip system is uniquely determined as the direction perpendicular to the dislocation line direction. The morphology of the dislocation substructures generated by CDD are then characterized with a method based on streamlines, which are obtained by travelling along a given vector field. The results demonstrate that CDD is a powerful tool that is capable of informing higher level crystal plasticity models.

2 Methodology

2.1 The vector-density based continuum dislocation dynamics

In CDD, it is assumed that dislocations locally have the same line direction at a given point in space, so the dislocation density vector can be viewed as a dislocation bundle. The assumption is satisfied by choosing a relatively small mesh. Following Nye (1953) and Kröner (1958), we express dislocation density tensor, α , as

$$\alpha = -\nabla \times \beta^p, \quad (6)$$

with β^p being the plastic distortion tensor. Both tensors can be decomposed into slip system contributions,

$$\alpha = \sum_k \alpha^{(k)}, \quad (7)$$

$$\beta^p = \sum_k \beta^{(k)}, \quad (8)$$

where k is a slip system index. As dislocations move, the plastic distortion will evolve and its time rate of change follows Orowan's law,

$$\dot{\beta}^{p(k)} = -v^{(k)} \times \alpha^{(k)}, \quad (9)$$

where $\mathbf{v}^{(k)}$ is the dislocation velocity on slip system k . Here, we assume the resolution is sufficiently fine such that the line direction of a dislocation segment is unique at each point in the crystal. As such, the direction of the dislocation velocity $\mathbf{v}^{(k)}$, which is perpendicular to the dislocation line is uniquely defined. The dislocation density vector $\boldsymbol{\rho}^{(k)}$ is used to represent the dislocation density and line direction at all points. The relation between the dislocation density vector $\boldsymbol{\rho}^{(k)}$ and the dislocation density tensor $\boldsymbol{\alpha}^{(k)}$ is stated as

$$\boldsymbol{\alpha}^{(k)} = \boldsymbol{\rho}^{(k)} \otimes \mathbf{b}^{(k)}, \quad (10)$$

where $\mathbf{b}^{(k)}$ is the Burgers vector of dislocations on slip system k . Combining Eqs. (6) through (10), the evolution equation for the dislocation density vector $\boldsymbol{\rho}^{(k)}$ in the absence of reactions and cross slip can be formulated as (Xia and El-Azab, 2015),

$$\dot{\boldsymbol{\rho}}^{(k)} = \nabla \times (\mathbf{v}^{(k)} \times \boldsymbol{\rho}^{(k)}). \quad (11)$$

In addition to the evolution of the dislocation density vector via dislocation glide described by Eq. (11), dislocation reactions among different slip systems also contribute to its evolution. Therefore, additional terms must be added to Eq. (11) to account for cross slip (Xia et al., 2016; Xia and El-Azab, 2015), collinear annihilation and junction reactions (Lin and El-Azab, 2020). Coupling these dislocation reactions with dislocation transport, the final form controlling the evolution of dislocations in CDD is

$$\dot{\boldsymbol{\rho}}^{(k)} = \nabla \times (\mathbf{v}^{(k)} \times \boldsymbol{\rho}^{(k)}) - \dot{\boldsymbol{\rho}}_{\text{cs}}^{(k,l)} + \dot{\boldsymbol{\rho}}_{\text{cs}}^{(l,k)} - \dot{\boldsymbol{\rho}}_{\text{col}}^{(k,l)} - \dot{\boldsymbol{\rho}}_{\text{g}}^{(kl,m)} + \dot{\boldsymbol{\rho}}_{\text{g}}^{(lm,k)} - \dot{\boldsymbol{\rho}}_{\text{L}}^{(kl,m)} - \dot{\boldsymbol{\rho}}_{\text{H}}^{(kl,m)} \quad (12)$$

where $\dot{\boldsymbol{\rho}}_{\text{cs}}^{(k,l)}$ and $\dot{\boldsymbol{\rho}}_{\text{cs}}^{(l,k)}$ are rate of change of dislocation density from and to slip system k due to cross slip, $\dot{\boldsymbol{\rho}}_{\text{col}}^{(k,l)}$ is the rate of change of dislocation density due to collinear annihilation, $\dot{\boldsymbol{\rho}}_{\text{g}}^{(kl,m)}$ accounts for the rate of change of dislocation density due to all glissile junctions with $\boldsymbol{\rho}^{(k)}$ as reactant, and $\dot{\boldsymbol{\rho}}_{\text{g}}^{(lm,k)}$ accounts for the rate of change of dislocation density due to all glissile junctions with $\boldsymbol{\rho}^{(k)}$ as product. The last two terms in Eq. (12) account for Lomer-Cottrell junction and Hirth junction formation. In this work, Eq. (12) only considers cross slip, collinear annihilation and glissile junctions to capture the dislocation density evolution. The effect of Lomer-Cottrell junction and Hirth junction to dislocation motion is considered via a Taylor law as described later (Eq. (20)).

The velocity field is required to solve Eq. (12). In the current model, the dislocation velocity is estimated by evaluating the internal long-range stress field from which the Peach-Koehler force for each slip system is evaluated then used to calculate the corresponding velocity via a dislocation mobility law. The long-range stress of the dislocations is calculated by solving the eigenstrain boundary value problem:

$$\begin{cases} \nabla \cdot \boldsymbol{\sigma} = \mathbf{0} & \text{in } V \\ \boldsymbol{\sigma} = \mathbf{C} : (\nabla \mathbf{u} - \boldsymbol{\beta}^p) & \text{in } V \\ \mathbf{u} = \bar{\mathbf{u}} & \text{on } \partial V_u \\ \mathbf{n} \cdot \boldsymbol{\sigma} = \bar{\mathbf{t}} & \text{on } \partial V_\sigma \end{cases}, \quad (13)$$

where $\boldsymbol{\sigma}$ is the Cauchy stress, \mathbf{C} is the symmetric, fourth rank elastic tensor, \mathbf{u} is the displacement field, $\boldsymbol{\beta}^p$ is the plastic distortion, \mathbf{n} is the unit normal to the traction boundary, ∂V_σ and ∂V_u , respectively, are the parts of the boundary over which the traction $\bar{\mathbf{t}}$ and the displacement $\bar{\mathbf{u}}$ boundary conditions are prescribed. The dislocation distortion $\boldsymbol{\beta}^p$ is updated by the field dislocation mechanics method (Acharya and Roy, 2006; Lin et al., 2021b; Roy and Acharya, 2006), expressed in the form $\boldsymbol{\beta}^p = \nabla \mathbf{z} - \boldsymbol{\chi}$, with $\nabla \mathbf{z}$ and $\boldsymbol{\chi}$ being the compatible and incompatible parts of $\boldsymbol{\beta}^p$, respectively. It has been shown that updating $\boldsymbol{\beta}^p$ by field dislocation mechanics is more accurate than directly integrating Orowan's equation (Lin et al., 2021b). These two components of the plastic distortion are governed by the following boundary value problems:

$$\begin{cases} \nabla \times \boldsymbol{\chi} = \sum_k \boldsymbol{\rho}^{(k)} \otimes \mathbf{b}^{(k)} & \text{in } V \\ \nabla \cdot \boldsymbol{\chi} = 0 & \text{in } V \\ \mathbf{n} \cdot \boldsymbol{\chi} = 0 & \text{on } \partial V \end{cases} \quad (14)$$

and,

$$\begin{cases} \nabla \cdot \nabla \dot{\mathbf{z}} = \nabla \cdot \sum_k (-\mathbf{v}^{(k)} \times \boldsymbol{\rho}^{(k)} \otimes \mathbf{b}^{(k)}) & \text{in } V \\ \mathbf{n} \cdot \nabla \dot{\mathbf{z}} = \mathbf{n} \cdot \sum_k (-\mathbf{v}^{(k)} \times \boldsymbol{\rho}^{(k)} \otimes \mathbf{b}^{(k)}) & \text{on } \partial V \\ \dot{\mathbf{z}} = \dot{\mathbf{z}}_o (\text{arbitrary value}) & \text{at one point in } V \end{cases} \quad (15)$$

Here, V is the simulation domain with boundary ∂V .

The dislocation velocity vector in Eq. (12) is expressed in the form

$$\mathbf{v}^{(k)} = v^{(k)} \boldsymbol{\eta}^{(k)} \quad (16)$$

with $v^{(k)}$ being the scalar velocity and $\boldsymbol{\eta}^{(k)}$ a unit vector in the direction of dislocation motion determined by the slip plane normal $\mathbf{m}^{(k)}$ and the dislocation line direction $\boldsymbol{\xi}^{(k)} = \boldsymbol{\rho}^{(k)} / \rho^{(k)}$ (Lin et al., 2021b),

$$\boldsymbol{\eta}^{(k)} = \mathbf{m}^{(k)} \times \boldsymbol{\xi}^{(k)}. \quad (17)$$

The scalar velocity $v^{(k)}$ is assumed to depend linearly on the resolved shear $\tau^{(k)}$ via the mobility law,

$$v^{(k)} = \text{sgn}(\tau^{(k)}) \frac{b}{B} [|\tau^{(k)}| - (\tau_0^{(k)} + \tau_p^{(k)})] \quad (18)$$

where $\text{sgn}(\cdot)$ returns the sign of its argument, $\tau^{(k)}$ is the resolved shear stress, b is the magnitude of the Burgers vector, B is the drag coefficient, and $\tau_0^{(k)}$ and $\tau_p^{(k)}$, respectively, are friction stress contributions due to lattice resistance and short-range interactions. In the above expression, $b\tau^{(k)}$ corresponds to the magnitude of the Peach-Koehler force (Peach and Koehler, 1950), and the resolved shear stress itself is given by

$$\tau^{(k)} = \mathbf{s}^{(k)} \cdot \boldsymbol{\sigma} \cdot \mathbf{m}^{(k)} \quad (19)$$

where $\mathbf{s}^{(k)} = \mathbf{b}^{(k)}/b$ is the unit slip direction. The resolved shear stress accounts for the long-range interactions between dislocations, dislocation-defect interactions, and boundary effects.

The friction stress $\tau_0^{(k)}$ is the threshold stress for dislocation motion (Hirth and Lothe, 1982; Hull and Bacon, 2011), while $\tau_p^{(k)}$ is the resistance caused by short-range interactions with dislocation junctions (Deng and El-Azab, 2010; El-Azab, 2000; Hochrainer, 2016; Sandfeld and Zaiser, 2015). In this work, $\tau_p^{(k)}$ is modelled using the Taylor hardening law proposed by (Devincre et al., 2006; Franciosi et al., 1980; Kubin et al., 2008) as

$$\tau_p^{(k)} = \mu b \sqrt{a^{kl} \rho^{(l)}} \quad (20)$$

with μ being the shear modulus and a^{kl} an interaction coefficient representing the average strength of the mutual interactions between slip systems k and l . As the collinear annihilation and glissile junction has been considered in Eq. (12), only sessile Lomer lock and Hirth junctions are considered in Eq. (20).

2.2 Mathematical description of streamlines in continuum dislocation dynamics

2D CDD simulations with only edge dislocations capture certain aspects of dislocation self-organization, which can be fully characterized in terms of the spatial density variations (Groma et al., 2003; Sandfeld and Zaiser, 2015; Wu et al., 2018). In the more realistic 3D CDD models, dislocations are curved lines and interact with one another to form complicated dislocation networks. Consequently, both the dislocation density and dislocation line direction become available for analysis and visualization of the dislocation substructure. Unlike the case of DDD

where dislocations are represented by discrete line segments, dislocation density fields are used in CDD. In such a representation, the dislocation lines are smeared and a technique is required to reconstruct dislocation lines from these field variables. Such a task can make use of the notion of streamlines, which are used in computational fluid dynamics to visualize fluid flows. Streamlines are families of curves that are locally tangent to the velocity vector in flowing fluids. In CDD, the dislocation density vector, which is analogous to the velocity field in fluid flow problems, can thus be analyzed using streamlines.

Let $P(s) = (x(s), y(s), z(s))$ represents the points on the streamlines of dislocations with coordinates (x, y, z) parameterized with the scalar distance s along the line. This parameterization satisfies

$$\frac{dx}{ds} = \frac{\rho_x(x,y,z)}{\|\boldsymbol{\rho}\|}, \quad \frac{dy}{ds} = \frac{\rho_y(x,y,z)}{\|\boldsymbol{\rho}\|}, \quad \frac{dz}{ds} = \frac{\rho_z(x,y,z)}{\|\boldsymbol{\rho}\|}. \quad (21)$$

where $\boldsymbol{\rho}$ is the dislocation density vector and ρ_x, ρ_y, ρ_z are the corresponding components. Given an initial point $P(0) = (x_0, y_0, z_0)$, it is possible to construct a series of points lying on the streamline passing through this initial point by solving the above set of differential equations. That is, we can reconstruct a series of points $P(s_1), P(s_2), P(s_3), \dots, P(s_n)$ along the streamline. Doing so for numerous suitably chosen initial points for the density of a given slip system makes it possible to visualize the entire dislocation population on that slip system. Coloring the streamline based on the local density magnitude also enables both the dislocation lines and their local densities throughout the crystal one slip system at a time.

A typical dislocation density substructure contains regions of low density and regions of high density (walls) that are impenetrable by mobile dislocation. The structure length scale along the glide direction of dislocations can be thus used to characterize the dislocation mean free path while the distance along the streamline of the dislocation between pinning points can be associated with the length of the mobile segments. These length scales can directly inform crystal plasticity models (Castelluccio et al., 2018; Castelluccio and McDowell, 2017); see also (Devincre et al., 2008).

A mobile dislocation segment length is defined as the distance between two pinning points along a dislocation line. Pinning points are defined as the points at which dislocation velocity is

smaller than a conveniently chosen small cutoff (tolerance), v_{tol} . Here it is taken to be 10^{-5} $\mu\text{m}/\text{ns}$. The mobile dislocation segment length, l_{mobile} , is then calculated using

$$l_{mobile} = \sum_{k=i}^{j-1} |s_{k+1} - s_k|, \text{ where} \\ \|\mathbf{v}(P(s_i))\| \leq v_{tol}, \quad \|\mathbf{v}(P(s_j))\| \leq v_{tol}, \text{ and} \\ \|\mathbf{v}(P(s_k))\| > v_{tol}, \quad i < k < j, \quad (22)$$

where s_k is the scalar distance along the density streamline at point k . In order to fix the mean free path of dislocations, it will be required to analyze the velocity of the dislocations in the direction of their glide. For this purpose, the dislocation trajectories (path lines) can be determined by the streamlines of the dislocation velocity field over short periods of time centered about the time of interest. As shown in Section 4.2.2, dislocation velocity fields do not significantly vary over the time that dislocations travel along their mean free path, which support the use of the dislocation movement path instead. If $Q(s) = (x(s), y(s), z(s))$ represents the points on the streamlines of dislocation velocity fields, these streamlines satisfy

$$\frac{dx}{ds} = \frac{v_x(x,y,z)}{\|\mathbf{v}\|}, \quad \frac{dy}{ds} = \frac{v_y(x,y,z)}{\|\mathbf{v}\|}, \quad \frac{dz}{ds} = \frac{v_z(x,y,z)}{\|\mathbf{v}\|}, \quad (23)$$

where \mathbf{v} is the dislocation velocity vector and v_x, v_y, v_z are the three components of \mathbf{v} . So, the dislocation mean free path, l_{free} , is calculated from

$$l_{free} = \sum_{k=i}^{j-1} |s_{k+1} - s_k|, \text{ where} \\ \|\mathbf{v}(Q(s_i))\| \leq v_{tol}, \quad \|\mathbf{v}(Q(s_j))\| \leq v_{tol}, \text{ and} \\ \|\mathbf{v}(Q(s_k))\| > v_{tol}, \quad i < k < j. \quad (24)$$

While Eqs. (22) and (24) give the structural quantities of interest, their analyses require density-weighting in order to properly average them.

3 Numerical implementation

The numerical implementation of CDD consists of solving the stress equilibrium problem for the displacement field \mathbf{u} given the plastic distortion field and solving the dislocation kinetics equations for all $\rho^{(k)}$. The plastic distortion is updated using the dislocation information by updating its compatible (\mathbf{z}) and incompatible (\mathbf{x}) parts and solving two subsidiary boundary value problems. A staggered scheme (Lin et al., 2021b; Xia and El-Azab, 2015) is used to decouple the mechanics and dislocation kinetic problems, which amounts to solving the mechanical equilibrium given the

plastic distortion, followed by an update for the dislocation evolution given the stress field. The solution scheme begins with the initialization of all slip systems with an initial dislocation density, which is then used to solve the field dislocation mechanics equations to obtain the corresponding plastic distortion β^p . Following this step, the stress field is obtained by solving the stress equilibrium equation, which is then used to obtain the dislocation velocity based on the mobility law. The velocity obtained is then used to solve the kinetic equation to update the dislocation density evolution. The new dislocation configuration is used for the next time step and the process is repeated until the average strain reaches the desired value. Two finite element methods are implemented to solve the overall problem. The mechanical equilibrium equations are solved using the Galerkin method (Belytschko et al., 2013) and the dislocation transport equations are solved using the first order systems least squares (FOSLS) method (Jiang, 2013), which enables the incorporation of the divergence-free constraints of the dislocation densities. An implicit Euler method (Press et al., 2007; Xia and El-Azab, 2015) is used for time discretization. The time step is controlled by a Courant-Friedrichs-Lewy condition (Lax, 1967), which ensures that the fastest dislocation line bundle cannot move through an entire element in one timestep. The streamline calculation is done by an implicit Runge-Kutta method (Press et al., 2007).

4 Results and discussion

4.1 The evolution of dislocation loops represented by streamlines

In this section, a simple example is setup to illustrate the difference between two representations of the dislocation substructures obtained from the dislocation density fields. One is the commonly used scalar dislocation density, and the other is the streamline of the vector dislocation densities as proposed in this paper. The example shows the annihilation of two dislocation loops, which are initially located on two collinear slip systems of an FCC crystal, $(111)[0\bar{1}1]$ and $(\bar{1}11)[0\bar{1}1]$, and expands with a prescribed constant dislocation velocity, as shown in Figure 1. Since the dislocation lines have the same Burgers vector but opposite line directions at the intersection part, they annihilate with each other and form a larger dislocation loop across two slip planes. The evolution of dislocations on the two slip systems is tracked by solving the transport equations for the two dislocation density fields $\rho^{(1)}$ and $\rho^{(2)}$. To show the results in 3D, one commonly used method is to calculate the scalar dislocation density ρ , which is defined as the norm of the vector dislocation

density $\|\rho^{(1)}\| + \|\rho^{(2)}\|$. The scalar dislocation density is shown in Figure 1(a) and Figure 1(c). Lower and higher dislocation regions are distinguished by the legend. Figure 1 demonstrates that the scalar dislocation density describes key features of the annihilation process but, by its nature, lacks the ability to show the directions of dislocation lines. To enhance our ability to perform analysis of the dislocation substructure, the streamlines of the dislocation density fields can be used as shown in Figure 1(b) and Figure 1(d). The arrows on the streamlines show the dislocation line directions as tangents of the streamlines. We remark that the streamlines are only used to show the directions of the curved dislocation lines and the number of the streamlines should not be interpreted as the actual number of dislocation lines.

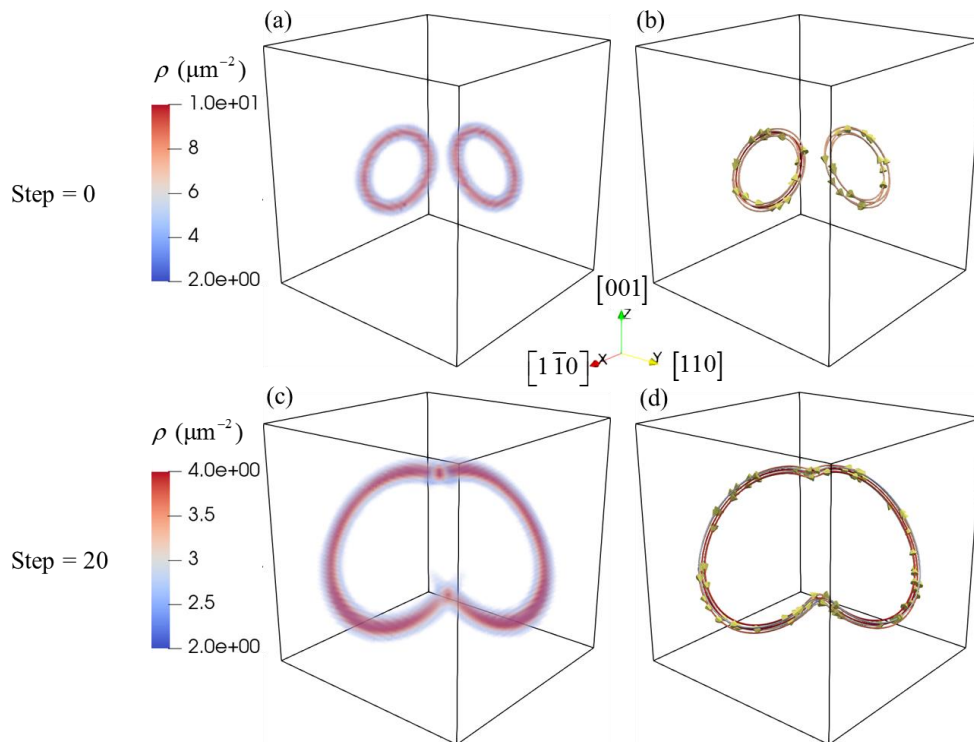


Figure 1. Collinear annihilation of two dislocation loops. (a), (c) Scalar density visualization. (b), (d) Streamline visualization.

4.2 The characteristics of dislocation substructures in a uniaxial loaded FCC crystal

In this section, a detailed analysis of the characteristics of dislocation substructures in a bulk simulation is performed using the streamlines of the dislocation density field. The simulation is

performed in a 5 μm cubic domain with all 12 slip systems of an FCC crystal considered. The edges of the simulation domain are along $[110]$, $[\bar{1}10]$ and $[001]$ crystallographic directions. The crystal is loaded along the $[001]$ direction with a strain rate of 20 s^{-1} . Periodic boundary conditions are applied on all faces of the domain. The material parameters for the simulations are: Young's modulus $E = 189 \text{ GPa}$, Poisson's ratio $\nu = 0.26$, Burgers vector $b = 0.254 \text{ nm}$, drag coefficient $B = 7.12 \times 10^{-6} \text{ Pa} \cdot \text{s}$. Initially, multiple dislocation loops are randomly placed in space, with periodic boundaries, on each slip system resulting in an initial dislocation density of $7.15 \times 10^{11} \text{ m}^{-2}$ distributed across all 12 slip systems and an initial radius ranging from $2 \mu\text{m}$ to $6 \mu\text{m}$. These parameters correspond to stainless steel (Déprés et al., 2004).

The stress strain curve for this case is shown in Figure 2(a). A typical elastoplastic response is observed, with an initial elastic regime followed by strain hardening. The analysis of dislocation substructure in the following section is performed at a number of snapshots of the dislocation microstructure in the plastic regime, labelled as A (0.12%), B (0.18%), C (0.30%), D (0.53%) and E (0.82%). The evolution of total dislocation density is shown in Figure 2(b). The dislocation density increases with strain.

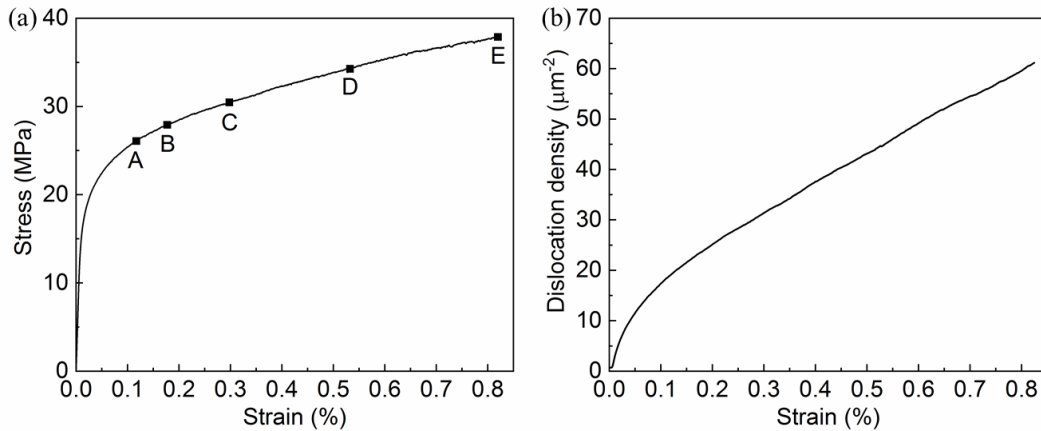


Figure 2. (a) The stress strain curve. (b) The evolution of total dislocation density.

The dislocation substructure on a $(1\bar{1}1)$ slip plane represented by the scalar dislocation density is shown Figure 3 for different strain levels. On average, the dislocation density increases with strain, and the distribution of dislocations evolves during loading. Within the small strain applied

here, there is no clear dislocation pattern yet. We now apply the streamline calculations to visualize and analyze the mobile dislocation population and the dislocation mean free paths.

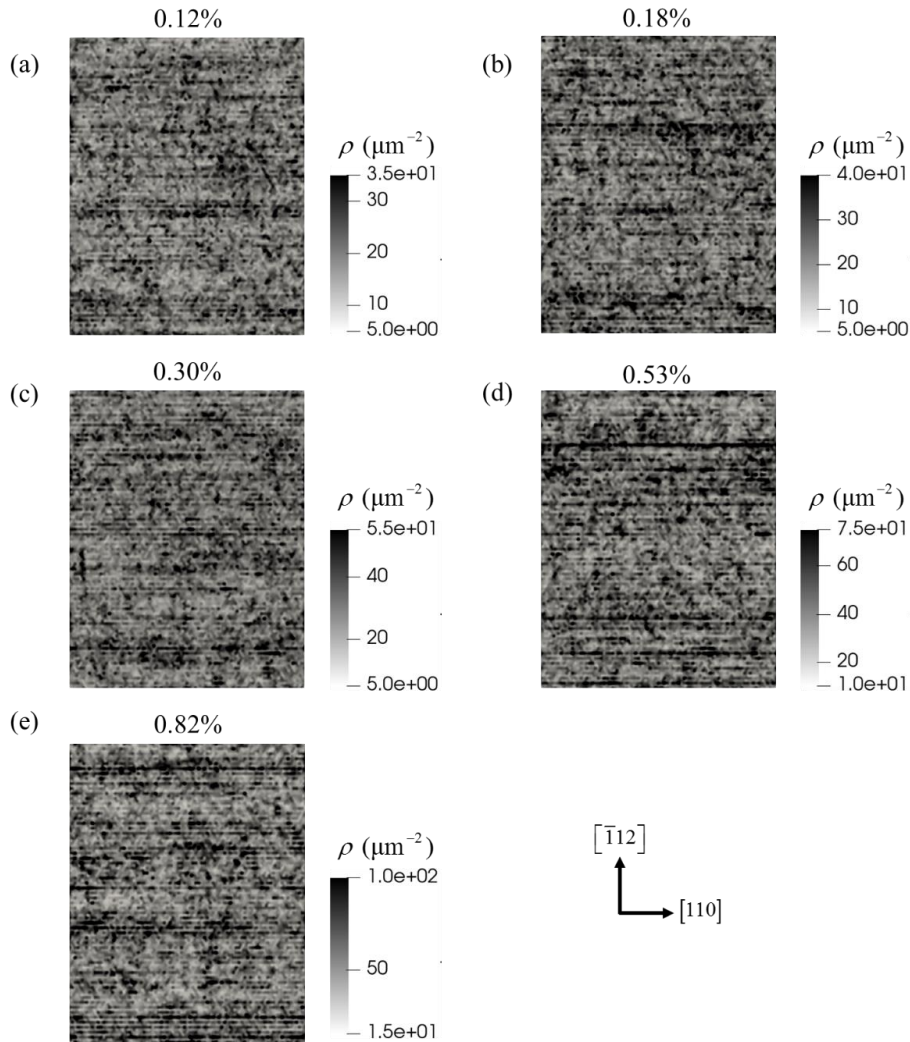


Figure 3. Distribution of total dislocation density at different strain on a $(1\bar{1}1)$ slip plane. The individual panels are $5 \mu\text{m}$ in width and $6.43 \mu\text{m}$ in height.

4.2.1 The evolution of mobile dislocation segment length

An adequate estimation of the mobile dislocation segment length is paramount for crystal plasticity models since this length scale controls the bow out strength of immobile edge dislocations bounded by two pinning points at dislocation walls (Castelluccio et al., 2018; Castelluccio and McDowell,

2017). In CDD models, the mobile dislocation segment length is computed by Eq. (21), which has been solved with an adaptive Runge-Kutta method. The calculations are performed to identify the dislocation substructure at five different strains as shown in Figure 3. For each slip system, 1000 initial seed points are used to calculate the streamlines. The seed points are not chosen arbitrarily but are on the mesh points where dislocation velocities are sufficiently high to be considered as mobile. The streamline calculation is done both downstream and upstream from the seed point with 2000 points in each direction along the streamline.

The streamlines of dislocations on slip system $(111)[0\bar{1}1]$ at 0.12% strain are shown in Figure 4, in which the color of each streamline represents the local dislocation velocity. Figure 4(a) shows the streamlines in the bulk; different from the scalar dislocation density representation (Figure 3), the curved nature of dislocations in 3D is well captured. A slice along the slip plane with thickness of 1 μm is taken from the bulk and is shown in Figure 4(b). To illustrate the details of the mobile dislocation segment, the configuration is enlarged by a factor of 4 and is shown in Figure 4(c). There are two types of mobile dislocation segments, labelled as A and B. Type A shows a spiral configuration, which corresponds to a single-arm dislocation source (Cui et al., 2014; Lin et al., 2015; Parthasarathy et al., 2007). The newly generated dislocation from the source is mobile. Type B is the segment on a long dislocation line. The local stress is high enough to make the segment mobile.

The statistics of the mobile segment lengths can be analyzed by extracting the mobile dislocation segments from Figure 4(a) based on the threshold dislocation velocity $v_{tol} = 10^{-5} \mu\text{m}/\text{ns}$ (0.01 ms^{-1}). A typical mobile dislocation segment configuration is illustrated in Figure 4(d), which corresponds to the same location as Figure 4(c). All immobile dislocation segments on the streamlines are removed.

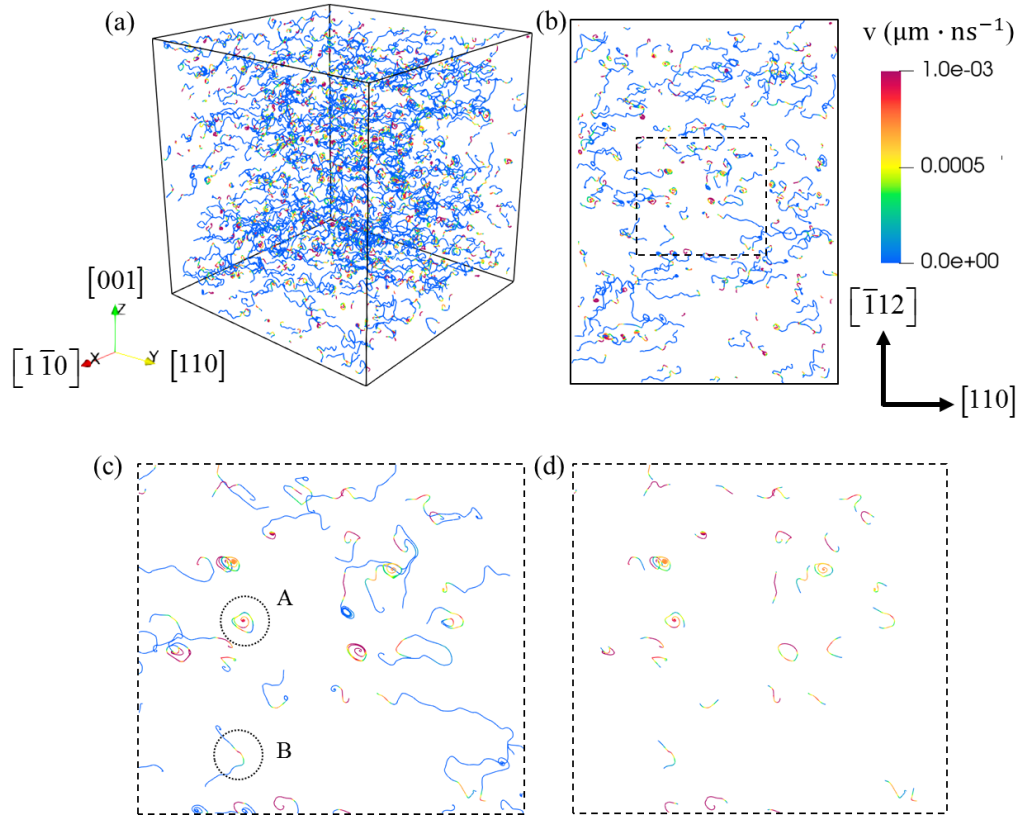


Figure 4. Streamlines of mobile dislocation segments on slip system $(111)[0\bar{1}1]$ at 0.12% strain. (a) Streamlines calculated in the bulk. (b) A slice taken from the bulk along the slip plane with thickness of $1 \mu\text{m}$. (c) Streamlines magnified by a factor of 4 from (b). (d) Mobile dislocation segments extracted from (c).

The length of the mobile dislocation segment varies throughout the simulation domain. Hence, we first calculate the length of each mobile dislocation segment, l_{mobile}^i and the dislocation density for that segment, ρ^i . A histogram is then used to show the distribution of l_{mobile}^i weighted by ρ^i . The reason for using ρ^i as the weight is that, the streamline only represents the line configuration but not the density. A higher local dislocation density at a given point means there are more mobile dislocations associated with the visualized streamline at that point. The distributions of the mobile dislocation segment length for all eight active slip systems (for the given loading direction) at 0.82% strain are shown in Figure 5. Notwithstanding minor differences among different slip systems, they all have similar probability density functions, which can be approximated by log-normal distribution,

$$P(l_{mobile}) = \frac{1}{l_{mobile}\sigma\sqrt{2\pi}} \exp\left(-\frac{(\ln(l_{mobile})-\mu)^2}{2\sigma^2}\right), \quad (25)$$

as shown in Figure 5. The log-normal distribution indicates that $\ln(l_{mobile})$ has a normal distribution, with mean μ and standard deviation σ . This distribution is often useful to describe stochastic processes in material science (Gruber et al., 2008; Keller et al., 1999) and dislocation source lengths in DDD simulations (Shishvan and Van der Giessen, 2010).

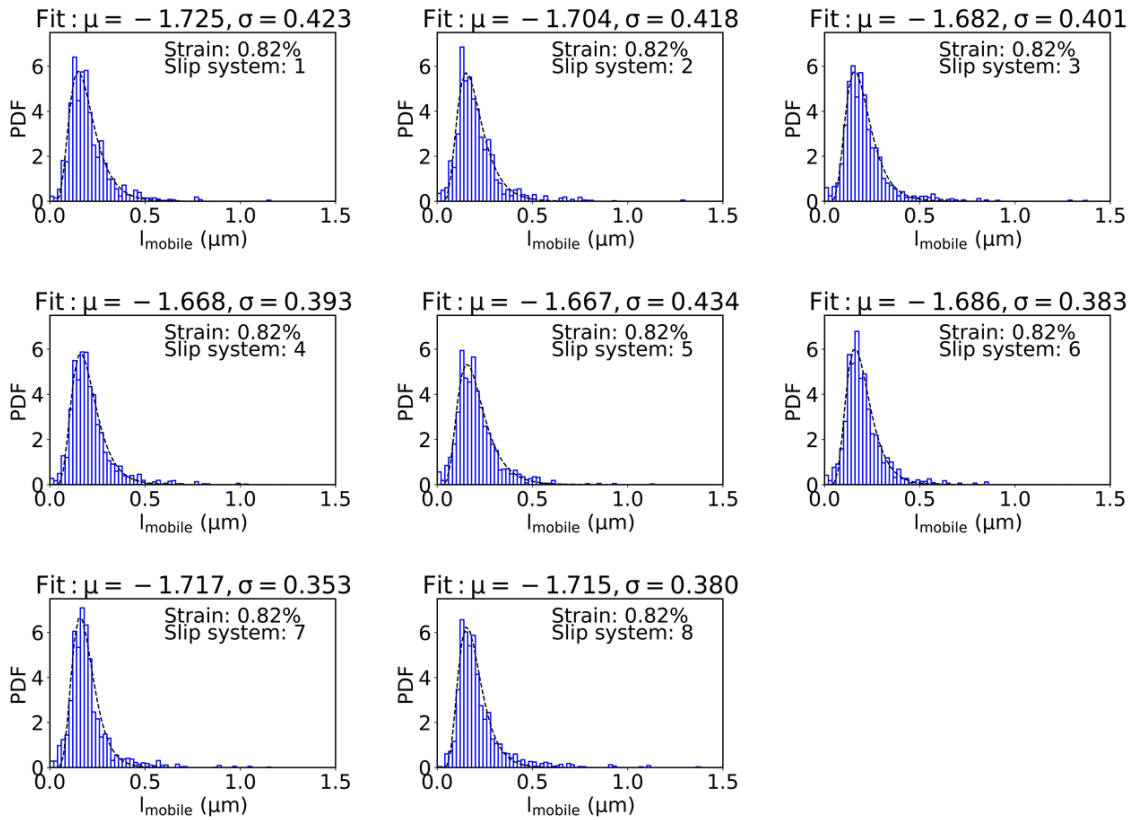


Figure 5. Distributions of mobile dislocation segment length for different slip systems at 0.82% strain. The data is plotted together with the log-normal fitting curves and the corresponding distribution parameters are listed on top of each panel.

The combined distribution of the mobile dislocation segment length is shown in Figure 6 at different strain levels. At each strain, the distribution is calculated by summing all mobile dislocation segments on all active slip systems. A clear trend of a decreasing mobile dislocation segment length is observed as the strain increases. At 0.12% strain, the mean value of the

distribution μ equal to -1.586 , which corresponds to a mobile segment length of $l_{mobile} = \exp(\mu) = 0.205 \mu\text{m}$. While at 0.82% strain, $\mu = -1.695$ corresponding to $l_{mobile} = \exp(\mu) = 0.184 \mu\text{m}$. We notice that the average mobile dislocation segment length becomes shorter as the strain increases, which is consistent with the fact that the mutual pinning of dislocations increases as the dislocation density increases. This observation can be validated by the forest hardening theories which predicts the distance between pinning points to vary as $\frac{1}{\sqrt{\rho}}$ where ρ is total dislocation density (Baird and Gale, 1965; Schoeck and Frydman, 1972; Kocks and Mecking, 2003). Since the total dislocation density increases with strain, the distance between the pinning points will decrease. Hence, one can expect the mobile dislocation segment length which is defined as the length of dislocation between two pinning points along the streamline to decrease with strain.

Another observation is that the standard deviation σ also decreases with increasing strain, which means that the distribution is less scattered at higher strain.

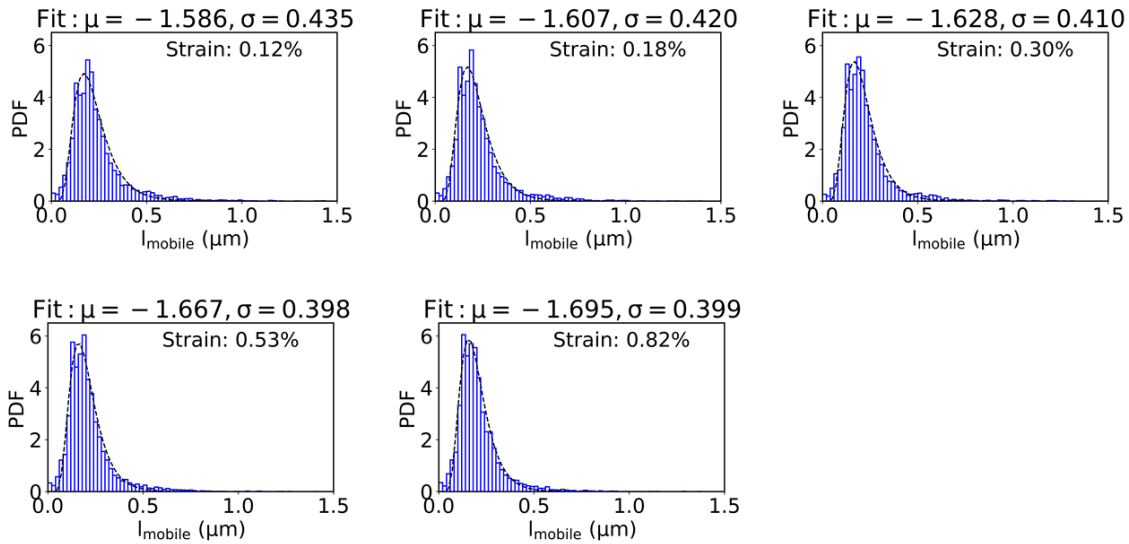


Figure 6. Distributions of mobile dislocation segment length at different strains. The data is plotted together with the log-normal fitting curves and the corresponding distribution parameters are listed on top of each panel.

Figure 7(a) summarizes the average mobile dislocation segment length as a function of strain. To further illustrate the results, Figure 7(b) plots the average mobile dislocation segment length

versus the inverse of the applied stress, which shows a nearly linear relation. These results demonstrate that the mean segment length decreases with increasing stress, following what appears as a similitude law. Other similitude laws in plasticity can be found in the relatively recent review (Sauzay and Kubin, 2011), which are material invariant in FCC metals. Shorter mobile dislocation segment length implies that the length of dislocation source is also shorter. As a result, higher applied stress are required to activate these dislocation sources (Balluffi, 2016; Hirth and Lothe, 1982).

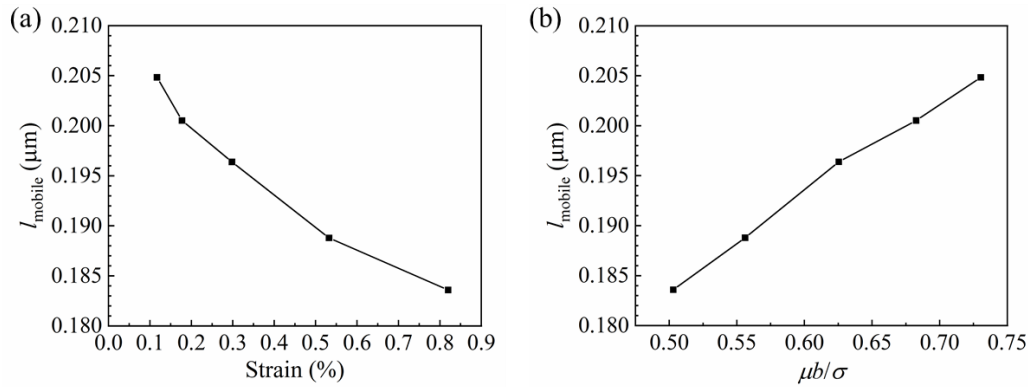


Figure 7. Mobile dislocation segment length versus (a) strain and (b) a scaled inverse of stress.

4.2.2 The evolution of dislocation mean free path

The mobile dislocations mean free path is another important length scale in crystal plasticity models since it controls the dislocation density evolution; basically, shorter mean free paths result in higher dislocation densities and more hardening. In DDD, the mean free path can be determined by explicitly tracking the individual dislocations and their blockage by other dislocations via junction formation (Devincre et al., 2008). In CDD, the dislocations mean free path can be detected by inspecting the dislocation velocity field. Basically, the mean free path (or free glide distance) of a dislocation segment can be defined as the distance over which the velocity remains above a certain threshold. This distance can be analyzed using the streamlines of the dislocation velocity field. In order to use the velocity field for this purpose, it must be monitored over the time the dislocation travels its free glide distance. However, it is possible to analyze the mean free path of the dislocations from a single snapshot of the velocity field if the velocity field does not change significantly over the time the mobile dislocations traverse their free glide distances. In order to

ensure that this is the case, we define and compare two characteristic time scales, the “rise time” and the “travel time.” The rise time is the time required for the dislocation velocity to change from immobile to mobile values at a specific location. The travel time is the time required for a mobile dislocation to travel along its mean free path. If the travel time is much smaller than the rise time, then the dislocation velocity field is said to evolve slowly, and the velocity field at a single snapshot of the dislocation configuration is adequate for computing the mean free path by searching for the distances between two pinning points along the trajectory of the dislocation line (streamline of the velocity field).

Dislocation velocities at $N = 10^4$ random points in the simulation domain are monitored during the deformation to analyze the rise time and travel time. The dislocation velocity profiles of ten sample points are shown in Figure 8. The dislocation velocities are sampled within strain intervals of $\pm 0.004\%$ at 0.12%, 0.18%, 0.30%, 0.53% and 0.82% strain. For an applied strain rate of 20 s^{-1} , the strain interval of 0.008% corresponds to $4\mu\text{s}$. The results show that velocity at some locations is above the threshold defining a mobile dislocation, with $v > 0.01 \text{ m/s}$. For example, three of the ten points have dislocation velocity in the mobile range over the strain interval 0.116%~0.124% (Figure 8(a)), while only one of the ten points have a dislocation velocity in the mobile range over the strain interval 0.526%~0.534% (Figure 8(d)).

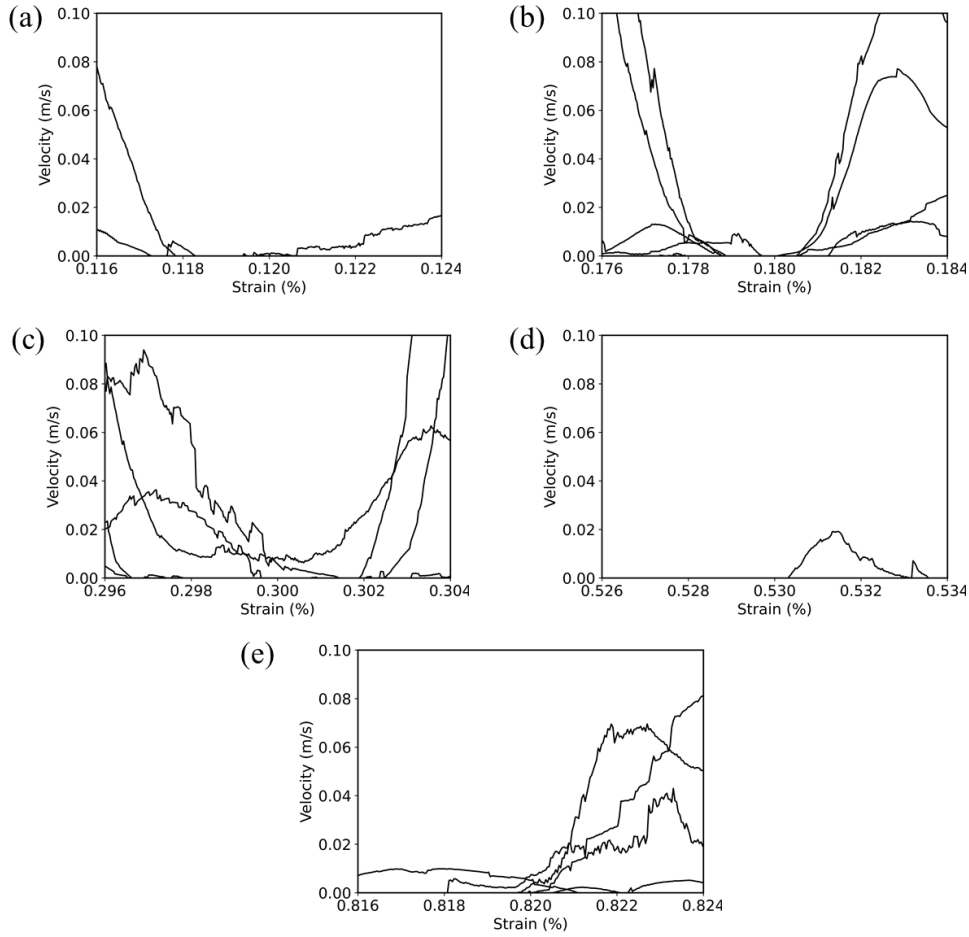


Figure 8. Evolution of the dislocation velocity at ten random points out of the 10^4 random points analyzed in the simulations. The velocity data is collected within strain interval $\pm 0.004\%$ at (a) 0.12%; (b) 0.18%; (c) 0.30%; (d) 0.53%; (e) 0.82% strain levels. The velocity at some points remain zero over the sampling intervals at various strain levels.

To quantitatively analyze how fast the dislocation velocities are changing, the rise time at the 10^4 sample points are calculated and its distribution at different strains are plotted in Figure 9. The vertical axis in this figure denotes fraction of points $n(t_{\text{rise}})/N$, where $n(t_{\text{rise}})$ is the number of points corresponding to a given rise time. We first pick the subset of all points with dislocation velocity less than the 0.01 m/s at each strain. Then we track the evolution of dislocation velocities at these points. A rise time is recorded when the dislocation velocity exceeds 0.01 m/s. If the dislocation velocity never exceeds 0.01 m/s over the monitoring interval, the rise time is recorded as 4×10^3 ns, which is the monitoring time itself. Figure 9 indicates that most of the initially

immobile dislocations remain immobile during the monitoring time and even for the dislocations that eventually become mobile, the rise time is larger than 2×10^3 ns. As we will show later, the mean free path is in the order of 10^2 nanometers, while the average dislocation velocity along the mean free path is typically in the order of 1 m/s. Thus, the travel time will be in the order of 10^2 ns – a factor of 20 shorter than the rise time. Therefore, it is possible to use velocity field at a single snapshot of the dislocation configuration to compute the mean free path with the help of the velocity streamline analysis. We remark here that this finding is consistent with the nature of dislocation ensembles in deforming crystals, that a large fraction of the dislocation density is immobile, and that, on average, dislocations remain in an immobile state for much longer times than in a mobile state.

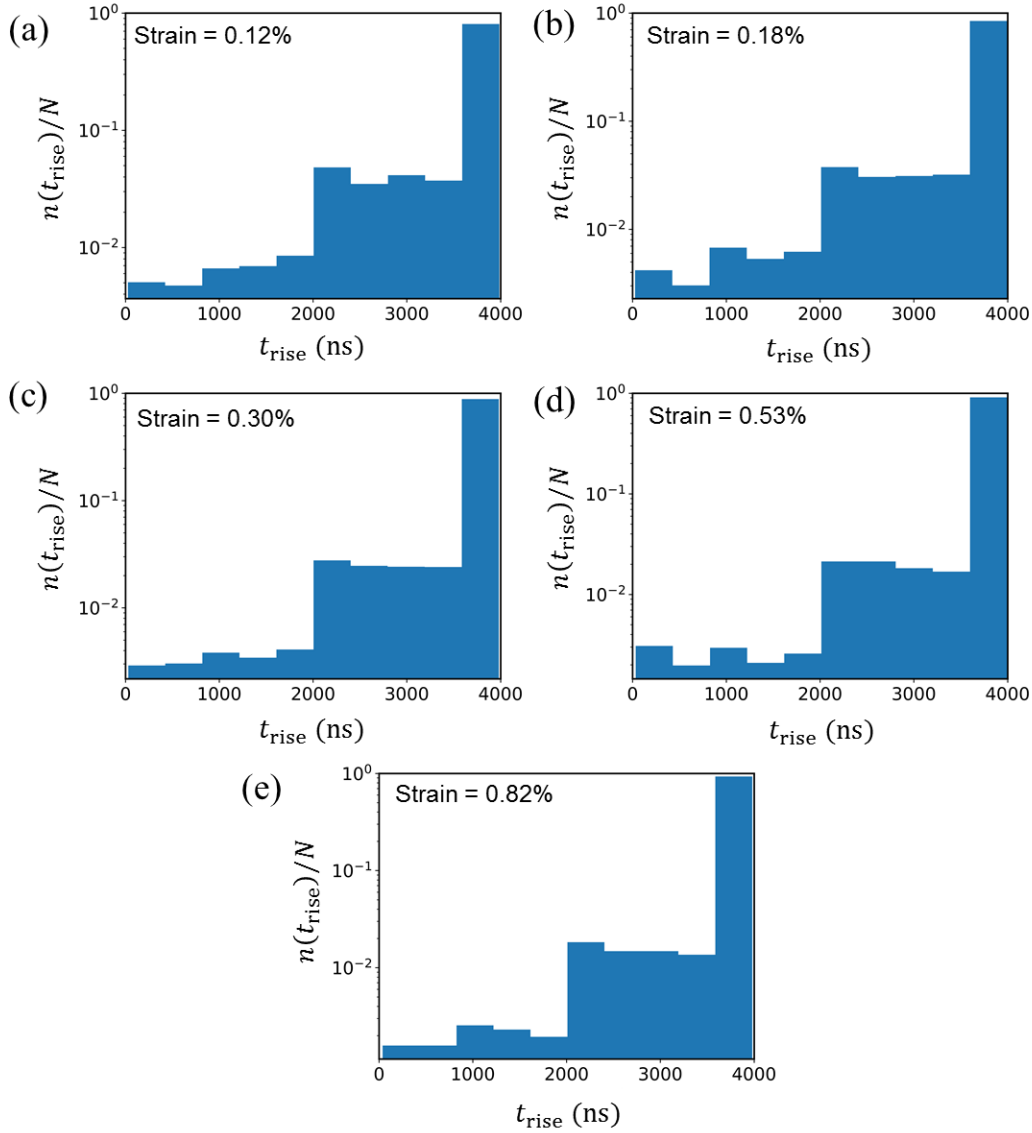


Figure 9. The histograms of rise time at 10^4 random points in the simulation domain at (a) 0.12%; (b) 0.18%; (c) 0.30%; (d) 0.53%; (e) 0.82% strain. The vertical axis records the fraction of points corresponding to each rise time.

We now proceed with the method of streamlines to calculate the dislocation mean free path using the approach discussed in Section 4.2.1. An adaptive Runge-Kutta method is used to solve Eq. (24) starting from 10^3 initial seed points. The resulting streamlines of dislocation mean free path are shown in Figure 10. Here, only the streamlines on slip system $(111)[0\bar{1}1]$ at 0.12% strain are shown as an example. The color on each streamline represents the local dislocation velocity which varies along the dislocation mean free path, with the highest value at the middle, which can

be as high as a few meters per second. Hence, the average dislocation velocity is approximated as half of the highest value, which was used to calculate the travel time. Comparing Figure 10 and Figure 4, the streamlines of dislocation mean free path are short and straight. This is consistent with discrete dislocation dynamics (DDD) simulation results (Stricker et al., 2018; Stricker and Weygand, 2015), where mobile dislocations were shown to be only able to move a relatively short distance before they react with other dislocations.

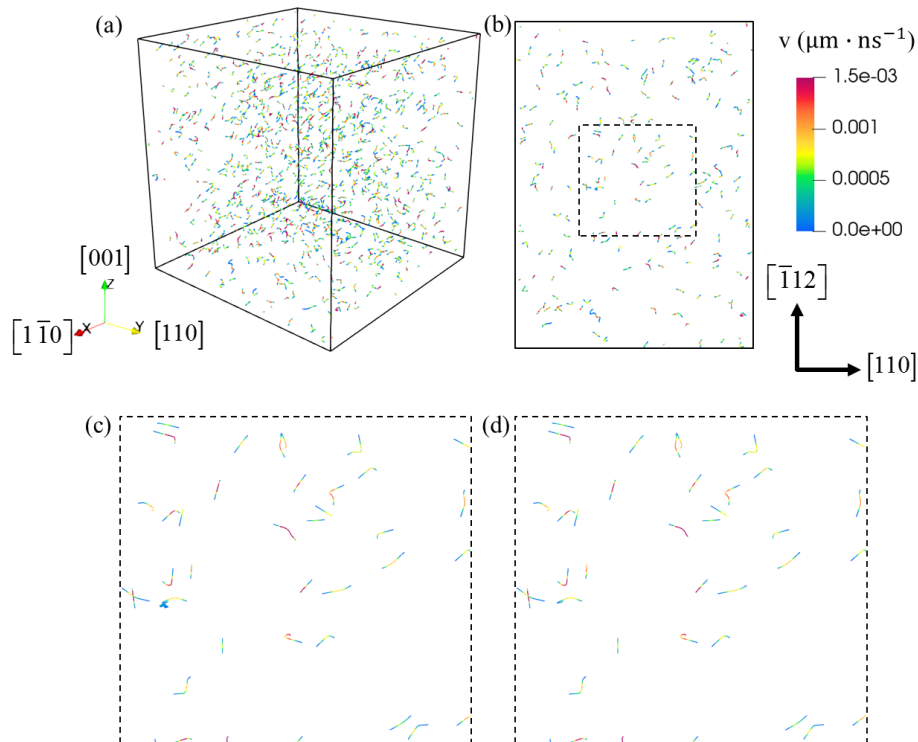


Figure 10. Streamlines of dislocation mean free path on slip system $(111)[0\bar{1}1]$ at 0.12% strain. (a) Streamlines calculated in the bulk. (b) A slice taken from the bulk along the slip plane with thickness of $1 \mu\text{m}$. (c) Streamlines magnified by a factor of 4 from (b). (d) Segments representing the dislocation mean free path extracted from (c).

The distributions of dislocation mean free path for all eight active slip systems at 0.82% strain are shown in Figure 11. It is estimated by first calculating the length of each segment of dislocation mean free path as shown in Figure 10(d) and the associated dislocation density. The histograms are then plotted by counting the number of points at a given mean free path, weighted by the dislocation density. Although there are slight differences among different slip systems, the shape of the distributions is quite similar. Unlike the log-normal distribution of mobile dislocation

segment length, the distribution of dislocation mean free path is more like a normal distribution, excluding the lower peak at about 50 nm, which is a distance on the order of the mesh size in our calculations. The largest mean free path observed is 400 nm, which spreads over 7~8 mesh elements and the majority of mobile dislocations seem to have a mean free path falling in the range 100~200 nm.

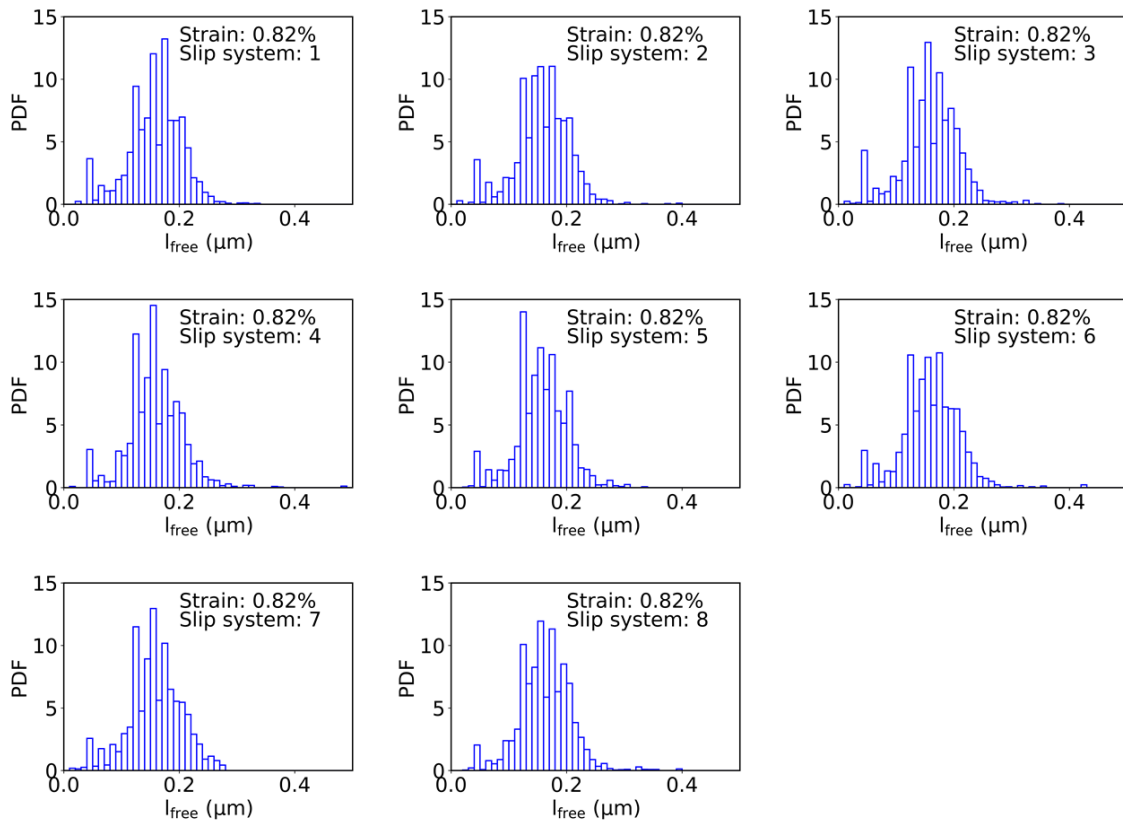


Figure 11. Distributions of dislocation mean free path for the eight active slip systems at 0.82% strain.

The distributions of dislocation mean free path at different strains are shown in Figure 12. For each strain, the distribution is calculated by summing all segments of dislocation mean free path on eight active slip systems. For all the dislocation configurations sampled at different strains in this simulation, dislocation mean free path is smaller than 400 nm and the most frequent glide distance is at about 160 nm. The shape of the distribution is similar at different strains. Figure 12 also shows that the range of dislocation mean free path decreases with increasing strain. For example, it spreads from 0~400 nm at 0.12% strain, while it spreads from 0~300 nm at 0.82% strain.

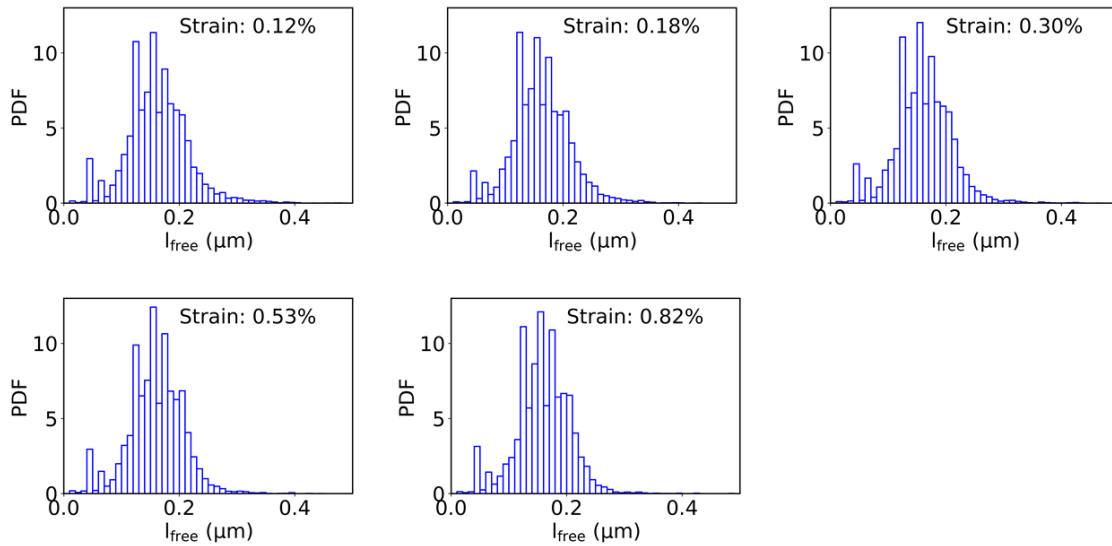


Figure 12. Distributions of dislocation mean free path at different strains.

Figure 13(a) shows that the average of dislocation mean free path decreases slightly but consistently with strain up 1% strain. The ratio of the mean free path to mobile dislocation segment length (η) is also plotted in Figure 13(b), which demonstrates that it steadily increases with strain. The results in Figure 13(b) lead to an important conclusion regarding the formation of dislocation substructures. The initial hardening follows more from the reduction of the mobile dislocation segment rather than the shortening of mean free paths. Thus, the initial production of dislocations works towards homogenizing the bow-out of dislocation segments and building a network of immobile dislocation density. As this mechanism becomes less efficient with the progressive homogenization of the structure (i.e., η in Figure 13(b) seems to saturate towards one), the role of the reduction of the dislocation mean free path becomes more significant.

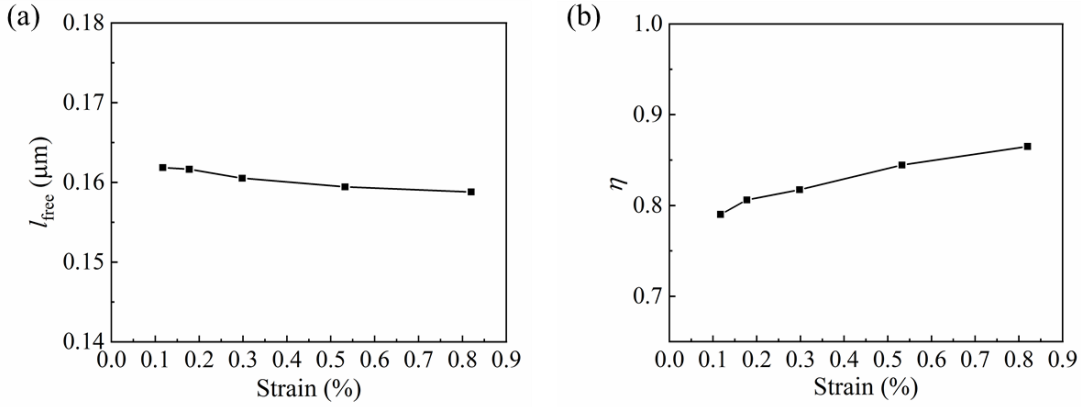


Figure 13. Dislocation mean free path and (b) the ratio $\eta = l_{free}/l_{mobile}$ versus strain.

4.2.3 Dislocation wall volume fraction

Another characteristic distance associated with the dislocation substructure is the wall thickness, which along with the structure spacing and length determines the wall volume fraction, f_w . Here, the wall volume fraction is calculated by assuming all immobile dislocations are constrained in dislocation walls. The dislocation wall volume is then obtained by summing the volume occupied by all immobile dislocations. The dislocation wall volume fraction versus strain is plotted in Figure 14 and found to vary between 0.26 and 0.40. Pham et al. (Pham and Holdsworth, 2014) reported f_w ranges between 0.1 and 0.7 depending on the stress and strain, which are consistent with our results. Furthermore, and aside from the strain range, the function form proposed by Estrin et al. (1998) for wall volume fraction evolution in Eq. (1) fits the dislocation wall volume fraction CDD data perfectly as can be seen in Figure 14. At small strains, structures are not clearly formed, and the dislocation walls are spread out, but the wall volume fraction gradually decreases upon further loading. This observation can be attributed to the general increase in local stress with the increase in resolved shear strain as it mobilizes the previously immobile dislocations resulting in the reduction of wall volume fraction.

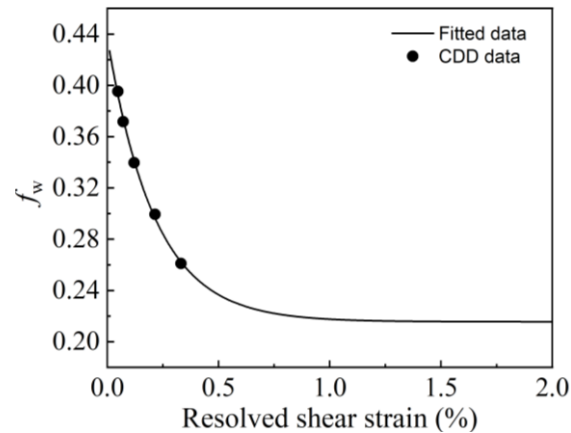


Figure 14. Dislocation wall volume fraction versus resolved shear strain.

5 Conclusion

Continuum dislocation dynamics is an effective method for simulating the evolution of dislocation substructures in crystalline materials. It has been applied to study dislocation pattern formation during deformation (Arora and Acharya, 2019; Groma et al., 2016; Sandfeld and Zaiser, 2015). However, most of these approaches are performed on two-dimensional dislocation ensembles. In this paper, the characteristics of three-dimensional dislocation substructures are analyzed by a vector density-based continuum dislocation dynamics, which is based on our earlier formulations (Lin et al., 2021b; Lin and El-Azab, 2020; Xia and El-Azab, 2015). In this model, dislocations on each slip system are represented by a vector field based on the dislocation bundle assumption. The dislocation density vectors carry the information of both the number of dislocation lines and the direction of these dislocation lines in a small representative volume. The evolution of the dislocation density vectors is controlled by a set of transport equations, coupled with the mechanical equilibrium equation. Finite element method is implemented to solve these equations.

Analyzing the three-dimensional dislocation substructure is challenging due to the curved nature of dislocation lines and their mutual interactions. A novel streamline method is proposed to obtain the characteristics of dislocation substructures generated by continuum dislocation dynamics. The streamlines can be established both for the dislocation lines and the dislocation

velocity. Streamlines are calculated by travelling along the given vector field starting at a suitably chosen set of initial points using an implicit Runge-Kutta method.

Substructure-sensitive crystal plasticity models rely on mesoscale parameterizations to quantify the underlying dislocation hardening mechanisms. Here, the streamline method is applied for a uniaxially loaded FCC crystal with eight active slip systems to analyze the evolution of the mobile dislocation segment length and dislocation mean free path. The results obtained from our analysis showed that both the average mobile segment length and the dislocation mean free path parameters decrease with increasing strain. In addition, our analysis also revealed that the ratio of mean free path to mobile dislocation segment length increases with strain. For a crystal oriented for loading along the [001] axis, the results have been successfully parameterized for the mobile dislocation segment length, the mobile dislocation mean free path, and the wall volume fraction. These results can be directly used to inform crystal plasticity models and support an effective strategy for bridging scale in bottom-up modelling approaches.

Further work with the CDD model proposed in this paper can shed light on multiscale crystal plasticity simulations. Substructure sensitive crystal plasticity models require a parameterization of the evolution of the characteristic scales of the dislocation substructures, which can be efficiently informed by CDD approaches. The streamline method developed in this paper is aimed at analyzing the characteristics of three-dimensional dislocation density vectors and serve as the bridge linking continuum dislocation dynamics to macroscopic crystal plasticity. Although the applied strain is limited to small strain under monotonic loading, the characteristics of dislocation substructure have been captured and the capabilities of the approach have been demonstrated.

Acknowledgements

The authors are grateful for the support from the Naval Nuclear Laboratory, operated by Fluor Marine Propulsion, LLC for the US Naval Reactors Program. The computational methodology and writing of the work were supported by the National Science Foundation, Division of Civil, Mechanical, and Manufacturing Innovation (CMMI), through award number 1663311 and by the US Department of Energy, Office of Science, Division of Materials Sciences and Engineering, through award number DE-SC0017718 at Purdue University.

References

- Acharya, A., Roy, A., 2006. Size effects and idealized dislocation microstructure at small scales: Predictions of a Phenomenological model of Mesoscopic Field Dislocation Mechanics: Part I. *J. Mech. Phys. Solids* 54, 1687–1710. <https://doi.org/10.1016/j.jmps.2006.01.009>
- Akhondzadeh, S., Bertin, N., Sills, R.B., Cai, W., 2021. Slip-free multiplication and complexity of dislocation networks in FCC metals. *Mater. Theory* 5, 2. <https://doi.org/10.1186/s41313-020-00024-y>
- Akhondzadeh, S., Sills, R.B., Bertin, N., Cai, W., 2020. Dislocation density-based plasticity model from massive discrete dislocation dynamics database. *J. Mech. Phys. Solids* 145, 104152. <https://doi.org/10.1016/j.jmps.2020.104152>
- Arora, R., Acharya, A., 2019. Dislocation pattern formation in finite deformation crystal plasticity. *Int. J. Solids Struct.* <https://doi.org/10.1016/j.ijsolstr.2019.02.013>
- Arsenlis, A., Parks, D.M., Becker, R., Bulatov, V. V., 2004. On the evolution of crystallographic dislocation density in non-homogeneously deforming crystals. *J. Mech. Phys. Solids* 52, 1213–1246. <https://doi.org/10.1016/j.jmps.2003.12.007>
- Ashraf, F., Castelluccio, G.M., 2021. A robust approach to parameterize dislocation glide energy barriers in FCC metals and alloys. *J. Mater. Sci.* 56, 16491–16509. <https://doi.org/10.1007/s10853-021-06376-1>
- Balluffi, R.W., 2016. *Introduction to Elasticity Theory for Crystal Defects*. World Scientific Publishing Company.
- Belytschko, T., Liu, W.K., Moran, B., Elkhodary, K., 2013. *Nonlinear finite elements for continua and structures*. John Wiley & Sons.
- Castelluccio, G.M., Geller, C.B., McDowell, D.L., 2018. A rationale for modeling hydrogen effects on plastic deformation across scales in FCC metals. *Int. J. Plast.* 111, 72–84. <https://doi.org/10.1016/j.ijplas.2018.07.009>
- Castelluccio, G.M., McDowell, D.L., 2017. Mesoscale cyclic crystal plasticity with dislocation substructures. *Int. J. Plast.* 98, 1–26. <https://doi.org/10.1016/j.ijplas.2017.06.002>
- Csikor, F.F., Motz, C., Weygand, D., Zaiser, M., Zapperi, S., 2007. Dislocation Avalanches, Strain Bursts, and the Problem of Plastic Forming at the Micrometer Scale. *Science* (80-.). 318, 251–254. <https://doi.org/10.1126/science.1143719>

- Cui, Y.N., Lin, P., Liu, Z.L., Zhuang, Z., 2014. Theoretical and numerical investigations of single arm dislocation source controlled plastic flow in FCC micropillars. *Int. J. Plast.* 55, 279–292. <https://doi.org/10.1016/j.ijplas.2013.11.011>
- Deng, J., El-Azab, A., 2010. Temporal statistics and coarse graining of dislocation ensembles. *Philos. Mag.* 90, 3651–3678. <https://doi.org/10.1080/14786435.2010.497472>
- Déprés, C., Robertson *, C.F., Fivel, M.C., 2004. Low-strain fatigue in AISI 316L steel surface grains: a three-dimensional discrete dislocation dynamics modelling of the early cycles I. Dislocation microstructures and mechanical behaviour. *Philos. Mag.* 84, 2257–2275. <https://doi.org/10.1080/14786430410001690051>
- Devincre, B., Hoc, T., Kubin, L., 2008. Dislocation Mean Free Paths and Strain Hardening of Crystals. *Science* (80-.). 320, 1745–1748. <https://doi.org/10.1126/science.1156101>
- Devincre, B., Kubin, L., Hoc, T., 2006. Physical analyses of crystal plasticity by DD simulations. *Scr. Mater.* 54, 741–746. <https://doi.org/10.1016/j.scriptamat.2005.10.066>
- El-Azab, A., 2000. Statistical mechanics treatment of the evolution of dislocation distributions in single crystals. *Phys. Rev. B - Condens. Matter Mater. Phys.* 61, 11956–11966. <https://doi.org/10.1103/PhysRevB.61.11956>
- Estrin, Y., Tóth, L.S., Molinari, A., Bréchet, Y., 1998. A dislocation-based model for all hardening stages in large strain deformation. *Acta Mater.* 46, 5509–5522. [https://doi.org/10.1016/S1359-6454\(98\)00196-7](https://doi.org/10.1016/S1359-6454(98)00196-7)
- Franciosi, P., Berveiller, M., Zaoui, A., 1980. Latent hardening in copper and aluminium single crystals. *Acta Metall.* 28, 273–283. [https://doi.org/10.1016/0001-6160\(80\)90162-5](https://doi.org/10.1016/0001-6160(80)90162-5)
- Grilli, N., Janssens, K.G.F., Nellessen, J., Sandlöbes, S., Raabe, D., 2018. Multiple slip dislocation patterning in a dislocation-based crystal plasticity finite element method. *Int. J. Plast.* 100, 104–121. <https://doi.org/10.1016/j.ijplas.2017.09.015>
- Groma, I., Csikor, F.F., Zaiser, M., 2003. Spatial correlations and higher-order gradient terms in a continuum description of dislocation dynamics. *Acta Mater.* 51, 1271–1281. [https://doi.org/10.1016/S1359-6454\(02\)00517-7](https://doi.org/10.1016/S1359-6454(02)00517-7)
- Groma, I., Zaiser, M., Ispánovity, P., 2016. Dislocation patterning in a two-dimensional continuum theory of dislocations. *Phys. Rev. B* 93, 214110. <https://doi.org/10.1103/PhysRevB.93.214110>

- Gruber, P.A., Böhm, J., Onuseit, F., Wanner, A., Spolenak, R., Arzt, E., 2008. Size effects on yield strength and strain hardening for ultra-thin Cu films with and without passivation: A study by synchrotron and bulge test techniques. *Acta Mater.* 56, 2318–2335. <https://doi.org/10.1016/j.actamat.2008.01.027>
- Hansen, N., Huang, X., 1998. Microstructure and flow stress of polycrystals and single crystals. *Acta Mater.* 46, 1827–1836. [https://doi.org/10.1016/S1359-6454\(97\)00365-0](https://doi.org/10.1016/S1359-6454(97)00365-0)
- Hansen, N., Huang, X., Pantleon, W., Winther, G., 2006. Grain orientation and dislocation patterns. *Philos. Mag.* 86, 3981–3994. <https://doi.org/10.1080/14786430600654446>
- Hirth, J., Lothe, J., 1982. *Theory of Dislocations*. John Wiley & Sons, New York.
- Hochrainer, T., 2016. Thermodynamically consistent continuum dislocation dynamics. *J. Mech. Phys. Solids* 88, 12–22. <https://doi.org/10.1016/j.jmps.2015.12.015>
- Hochrainer, T., 2015. Multipole expansion of continuum dislocations dynamics in terms of alignment tensors. *Philos. Mag.* 95, 1321–1367. <https://doi.org/10.1080/14786435.2015.1026297>
- Hull, D., Bacon, D.J., 2011. *Introduction to dislocations*. Butterworth-Heinemann.
- Jiang, B., 2013. *The least-squares finite element method: theory and applications in computational fluid dynamics and electromagnetics*. Springer Science & Business Media.
- Jiang, J., Benjamin Britton, T., Wilkinson, A.J., 2015. Evolution of intragranular stresses and dislocation densities during cyclic deformation of polycrystalline copper. *Acta Mater.* 94, 193–204. <https://doi.org/10.1016/j.actamat.2015.04.031>
- Keller, R.-M., Baker, S.P., Arzt, E., 1999. Stress–temperature behavior of unpassivated thin copper films. *Acta Mater.* 47, 415–426. [https://doi.org/10.1016/S1359-6454\(98\)00387-5](https://doi.org/10.1016/S1359-6454(98)00387-5)
- Kosevich, A.M., 1965. DYNAMICAL THEORY OF DISLOCATIONS. *Sov. Phys. Uspekhi* 7, 837–854. <https://doi.org/10.1070/PU1965v007n06ABEH003688>
- Kröner, E., 1958. *Kontinuums theorie der Versetzungen und Eigenspannungen*. Springer.
- Kubin, L., Devincere, B., Hoc, T., 2008. Toward a physical model for strain hardening in fcc crystals. *Mater. Sci. Eng. A* 483–484, 19–24. <https://doi.org/10.1016/j.msea.2007.01.167>
- Lavenstein, S., El-Awady, J.A., 2019. Micro-scale fatigue mechanisms in metals: Insights gained from small-scale experiments and discrete dislocation dynamics simulations. *Curr. Opin. Solid State Mater. Sci.* 23, 100765. <https://doi.org/10.1016/j.cossms.2019.07.004>

- Lax, P.D., 1967. Hyperbolic Difference Equations: A Review of the Courant-Friedrichs-Lewy Paper in the Light of Recent Developments. *IBM J. Res. Dev.* 11, 235–238.
<https://doi.org/10.1147/rd.112.0235>
- Leung, H.S., Leung, P.S.S., Cheng, B., Ngan, A.H.W., 2015. A new dislocation-density-function dynamics scheme for computational crystal plasticity by explicit consideration of dislocation elastic interactions. *Int. J. Plast.* 67, 1–25.
<https://doi.org/10.1016/j.ijplas.2014.09.009>
- Lin, P., El-Azab, A., 2020. Implementation of annihilation and junction reactions in vector density-based continuum dislocation dynamics. *Model. Simul. Mater. Sci. Eng.* 28, 045003.
<https://doi.org/10.1088/1361-651X/ab7d90>
- Lin, P., Liu, Z., Cui, Y., Zhuang, Z., 2015. A stochastic crystal plasticity model with size-dependent and intermittent strain bursts characteristics at micron scale. *Int. J. Solids Struct.* 69–70, 267–276. <https://doi.org/10.1016/j.ijsolstr.2015.05.024>
- Lin, P., Vivekanandan, V., Anglin, B., Geller, C., El-Azab, A., 2021a. Incorporating point defect generation due to jog formation into the vector density-based continuum dislocation dynamics approach. *J. Mech. Phys. Solids* 156, 104609.
<https://doi.org/10.1016/j.jmps.2021.104609>
- Lin, P., Vivekanandan, V., Starkey, K., Anglin, B., Geller, C., El-Azab, A., 2021b. On the computational solution of vector-density based continuum dislocation dynamics models: A comparison of two plastic distortion and stress update algorithms. *Int. J. Plast.* 138, 102943.
<https://doi.org/10.1016/j.ijplas.2021.102943>
- Monavari, M., Zaiser, M., 2018. Annihilation and sources in continuum dislocation dynamics. *Mater. Theory* 2, 3. <https://doi.org/10.1186/s41313-018-0010-z>
- Mughrabi, H., 1983. Dislocation wall and cell structures and long-range internal stresses in deformed metal crystals. *Acta Metall.* 31, 1367–1379. [https://doi.org/10.1016/0001-6160\(83\)90007-X](https://doi.org/10.1016/0001-6160(83)90007-X)
- Mura, T., 1963. Continuous distribution of moving dislocations. *Philos. Mag.* 8, 843–857.
<https://doi.org/10.1080/14786436308213841>
- Nye, J.F., 1953. Some geometrical relations in dislocated crystals. *Acta Metall.* 1, 153–162.
[https://doi.org/10.1016/0001-6160\(53\)90054-6](https://doi.org/10.1016/0001-6160(53)90054-6)

- Parthasarathy, T.A., Rao, S.I., Dimiduk, D.M., Uchic, M.D., Trinkle, D.R., 2007. Contribution to size effect of yield strength from the stochastics of dislocation source lengths in finite samples. *Scr. Mater.* 56, 313–316. <https://doi.org/10.1016/j.scriptamat.2006.09.016>
- Peach, M., Koehler, J.S., 1950. The Forces Exerted on Dislocations and the Stress Fields Produced by Them. *Phys. Rev.* 80, 436–439. <https://doi.org/10.1103/PhysRev.80.436>
- Pham, M.-S., Holdsworth, S.R., 2014. Evolution of Relationships Between Dislocation Microstructures and Internal Stresses of AISI 316L During Cyclic Loading at 293 K and 573 K (20 °C and 300 °C). *Metall. Mater. Trans. A* 45, 738–751. <https://doi.org/10.1007/s11661-013-1981-7>
- Press, W., Teukolsky, S., Vetterling, W., Flannery, B., 2007. Numerical recipes 3rd edition: The art of scientific computing. Cambridge University Press.
- Rafiei, M.H., Gu, Y., El-Awady, J.A., 2020. Machine Learning of Dislocation-Induced Stress Fields and Interaction Forces. *JOM* 72, 4380–4392. <https://doi.org/10.1007/s11837-020-04389-w>
- Reuber, C., Eisenlohr, P., Roters, F., Raabe, D., 2014. Dislocation density distribution around an indent in single-crystalline nickel: Comparing nonlocal crystal plasticity finite-element predictions with experiments. *Acta Mater.* 71, 333–348. <https://doi.org/10.1016/j.actamat.2014.03.012>
- Roy, A., Acharya, A., 2006. Size effects and idealized dislocation microstructure at small scales: Predictions of a Phenomenological model of Mesoscopic Field Dislocation Mechanics: Part II. *J. Mech. Phys. Solids* 54, 1711–1743. <https://doi.org/10.1016/j.jmps.2006.01.012>
- Sandfeld, S., Zaiser, M., 2015. Pattern formation in a minimal model of continuum dislocation plasticity. *Model. Simul. Mater. Sci. Eng.* 23, 065005. <https://doi.org/10.1088/0965-0393/23/6/065005>
- Sauzay, M., 2008. Analytical modelling of intragranular backstresses due to deformation induced dislocation microstructures. *Int. J. Plast.* 24, 727–745. <https://doi.org/10.1016/j.ijplas.2007.07.004>
- Sauzay, M., Kubin, L.P., 2011. Scaling laws for dislocation microstructures in monotonic and cyclic deformation of fcc metals. *Prog. Mater. Sci.* 56, 725–784. <https://doi.org/10.1016/j.pmatsci.2011.01.006>

- Shishvan, S.S., Van der Giessen, E., 2010. Distribution of dislocation source length and the size dependent yield strength in freestanding thin films. *J. Mech. Phys. Solids* 58, 678–695. <https://doi.org/10.1016/j.jmps.2010.02.011>
- Song, H., Gunkelmann, N., Po, G., Sandfeld, S., 2021. Data-mining of dislocation microstructures: concepts for coarse-graining of internal energies. *Model. Simul. Mater. Sci. Eng.* 29, 035005. <https://doi.org/10.1088/1361-651X/abdc6b>
- Steinberger, D., Song, H., Sandfeld, S., 2019. Machine Learning-Based Classification of Dislocation Microstructures. *Front. Mater.* 6. <https://doi.org/10.3389/fmats.2019.00141>
- Stricker, M., Sudmanns, M., Schulz, K., Hochrainer, T., Weygand, D., 2018. Dislocation multiplication in stage II deformation of fcc multi-slip single crystals. *J. Mech. Phys. Solids* 119, 319–333. <https://doi.org/10.1016/j.jmps.2018.07.003>
- Stricker, M., Weygand, D., 2015. Dislocation multiplication mechanisms - Glissile junctions and their role on the plastic deformation at the microscale. *Acta Mater.* 99, 130–139. <https://doi.org/10.1016/j.actamat.2015.07.073>
- Vivekanandan, V., Lin, P., Winther, G., El-Azab, A., 2021. On the implementation of dislocation reactions in continuum dislocation dynamics modeling of mesoscale plasticity. *J. Mech. Phys. Solids* 149, 104327. <https://doi.org/10.1016/j.jmps.2021.104327>
- Wu, R., Tüzes, D., Ispánovity, P.D., Groma, I., Hochrainer, T., Zaiser, M., 2018. Instability of dislocation fluxes in a single slip: Deterministic and stochastic models of dislocation patterning. *Phys. Rev. B* 98, 054110. <https://doi.org/10.1103/PhysRevB.98.054110>
- Wu, R., Zaiser, M., 2021. Cell structure formation in a two-dimensional density-based dislocation dynamics model. *Mater. Theory* 5, 3. <https://doi.org/10.1186/s41313-020-00025-x>
- Xia, S., Belak, J., El-Azab, A., 2016. The discrete-continuum connection in dislocation dynamics: I. Time coarse graining of cross slip. *Model. Simul. Mater. Sci. Eng.* 24, 075007. <https://doi.org/10.1088/0965-0393/24/7/075007>
- Xia, S., El-Azab, A., 2015. Computational modelling of mesoscale dislocation patterning and plastic deformation of single crystals. *Model. Simul. Mater. Sci. Eng.* 23, 055009. <https://doi.org/10.1088/0965-0393/23/5/055009>
- Yang, Z., Papanikolaou, S., Reid, A.C.E., Liao, W., Choudhary, A.N., Campbell, C., Agrawal, A., 2020. Learning to Predict Crystal Plasticity at the Nanoscale: Deep Residual Networks

and Size Effects in Uniaxial Compression Discrete Dislocation Simulations. *Sci. Rep.* 10, 8262. <https://doi.org/10.1038/s41598-020-65157-z>